



Catalytic combustion of lean methane over different Co_3O_4 nanoparticle catalysts

Panpan Zhang, Jinghua Liu, Chunjing Zhou, Zebin Xue, Yifan Zheng, Haodong Tang, Zongjian Liu*

College of Chemical Engineering, Zhejiang University of Technology, Hangzhou, 310014, PR China

ARTICLE INFO

Keywords:

Co_3O_4 nanoparticles
Catalytic combustion
Methane
Mesoporous SiO_2
Anti-sintering

ABSTRACT

Three types of Co_3O_4 catalyst, namely Co_3O_4 nanoparticles (denoted as Co_3O_4 -NPs, ~ 12 nm in diameter), Co_3O_4 nanoparticles encapsulated in mesoporous SiO_2 (denoted as $\text{Co}_3\text{O}_4@ \text{SiO}_2$), and Co_3O_4 nanoparticles inside microporous SiO_2 hollow sub-microspheres (denoted as Co_3O_4 -in- SiO_2), were explored to catalyze the combustion of lean methane. It was found that the methane conversion over the three catalysts has the order of Co_3O_4 -NPs $\approx \text{Co}_3\text{O}_4@ \text{SiO}_2 > \text{Co}_3\text{O}_4$ -in- SiO_2 due to the different catalyst structure. The comparison experiments at high temperatures indicate the $\text{Co}_3\text{O}_4@ \text{SiO}_2$ has a significantly improved anti-sintering performance. Combined with the TEM and BET measurements, the results prove that the presence of the mesoporous SiO_2 layer can maintain the catalytic activity and significantly improve the anti-sintering performance of $\text{Co}_3\text{O}_4@ \text{SiO}_2$. In contrast, the microporous SiO_2 layer reduces the catalytic activity of Co_3O_4 -in- SiO_2 possibly due to its less effective diffusion path of combustion product. Thus, the paper demonstrates the pore size of SiO_2 layer and catalyst structure are both crucial for the catalytic activity and stability.

1. Introduction

Natural gas is a cleaner fuel than its counterparts such as coal and oil. In the case of generating an equal amount of energy, for example, burning natural gas produces fewer air pollutants and CO_2 than burning coal or oil. Although natural gas has lagged behind coal and oil as an energy source for decades, its consumption has grown rapidly in last two decades [1–4]. However, methane, the dominant component of natural gas, is the second most dangerous greenhouse gas [5–7]. Moreover, methane is a very stable molecule and requires high energy to activate it and thus is difficult to be completely oxidized [8–10]. With increasing consumption of natural gas in recent decades the incomplete combustion of natural gas which may lead to direct emission of methane into atmosphere becomes a great threat to environment [5,6,11,12]. Though flame combustion usually induces complete oxidation of methane, it suffers from very high reaction temperature and emission of more dangerous pollutants (e.g., NO_x) [13,14]. As a result, the search for an efficient and environmentally friendly approach to complete oxidation of methane is of great importance [15].

As a highly promising alternative to flame combustion, catalytic combustion of methane has been recognized as one of the most efficient methods for the removal of methane due to its low operating temperature and has drawn extensive attention in the past [16–26]. The key issue in this method is to develop a highly active catalyst with long lifetime. In general, there are two types of

* Corresponding author.

E-mail address: zjliu@zjut.edu.cn (Z. Liu).

catalysts used in catalytic combustion of methane: supported noble metals (e.g., Pd and Pt) [17–20,27] and transition metal oxides (e.g., NiO, CuO, Mn₂O₃, and Co₃O₄) [17,21–26,28–32]. Although supported noble metal catalysts possess superior catalytic activity for complete oxidation of methane, the high cost and poor anti-sintering ability limit their practical applications. Among the second type of catalysts (namely transition metal oxides), Co₃O₄, a spinel type oxide, exhibits high activity for catalytic combustion of lean methane due to its high redox ability and strong oxygen mobility and has drawn increasing attention recently [23,26,28–30,33,34]. A great number of studies have reported that the surface and bulk character of Co₃O₄ catalysts also can be changed by utilizing different synthesis routes, doping second metal or changing the oxide support et al., resulting in the high catalyst reducibility and different chemical behavior [35–42].

So far, the reported experimental investigations on Co₃O₄ catalyst mainly focused on the following two aspects: (i) the effects of morphology and crystal plane of Co₃O₄ on the catalytic activity. Hu et al. for example, employed Co₃O₄ nanosheets, nanobelts, and nanocubes as the catalysts for methane combustion and found that the catalytic activity order of crystal planes follows {112} > {011} > {001} [23]. Chen et al. revealed a similar result that Co₃O₄ catalysts containing {111} planes possess higher performance than those containing {100} planes as dominantly exposed planes [24]. Sun et al. investigated Co₃O₄ with different dimensional architectures including nanoparticles, nanorods, nanoplates, and mesoporous and microporous structures and proved that Co₃O₄ nanoplates had the highest activity due to their exposed high-index planes and abundant surface-active species [25]; (ii) the effects of preparation conditions on the catalytic activity of Co₃O₄ nanoparticles. For instance, Zheng et al. prepared Co₃O₄ nanoparticles via a precipitation method and found that the pH values used in the precipitation process could change the concentrations of tetrahedral sites of Co²⁺ and surface-active oxygen species of the resulting Co₃O₄ nanoparticles, and thus had an important impact on their catalytic performance and long-term stability [28]. They also prepared Co₃O₄ catalysts using four different cobalt precursors, namely Co(C₂H₃O₂)₂, Co(NO₃)₂, CoCl₂, and CoSO₄, and demonstrated that Co₃O₄ nanoparticles from cobalt acetate owned a higher concentration of tetrahedral sites of Co²⁺, more surface-active oxygen species and better reducibility than those from other cobalt precursors, and consequently exhibited a better catalytic performance for combustion of methane [29]. Generally, the reaction temperature for 100 % conversion of CH₄ over Co₃O₄ catalysts is above 450 °C [28–30], which indicates that the thermal stability of Co₃O₄ catalysts at high temperatures is also important for complete combustion of methane. Thermodynamically, sintering of nano-sized particles readily occurs at high temperatures and therefore the development of Co₃O₄ catalyst with excellent thermal stability is also crucial for its practical application in complete oxidation of methane.

SiO₂ encapsulated metal catalysts (e.g., Ni–Cu and Ru nanoparticles) have been found to show high thermal stability for methane dry reforming [31,32], but there is few work on SiO₂ encapsulated Co₃O₄ nanoparticles for complete oxidation of methane. In this article, three types of Co₃O₄ catalysts, namely Co₃O₄ nanoparticles (denoted as Co₃O₄-NPs), Co₃O₄ nanoparticles encapsulated in mesoporous SiO₂ (denoted as Co₃O₄@SiO₂), and Co₃O₄ nanoparticles inside hollow SiO₂ sub-microspheres (denoted as Co₃O₄-in-SiO₂), were prepared and used to catalyze the combustion of lean methane. The main purpose of this article is to reveal the effects of SiO₂ layer on the thermal stability and catalytic performance of Co₃O₄ nanoparticles.

2. Materials and methods

2.1. Materials and chemicals

All chemicals were used as received. Except carboxymethylcellulose sodium (Chemical pure, 300–800 mPa s), all other chemicals were of analytical grade. Ethanol was purchased from Anhui Ante Food Co. Ltd. Tetraethoxysilane (TEOS), 3-aminopropyl triethoxysilane (APTES) and hydrogen peroxide were supplied from Shanghai McLean Biochemical Technology Co., Ltd. Ammonia was bought from Hangzhou Longshan Fine Chemical Co., Ltd. Carboxymethylcellulose sodium and oleic acid were provided from Aladdin Chemical Reagent Co., Ltd. All other reagents were obtained from Shanghai Guoyao Group Chemical Reagent Co., Ltd.

2.2. Preparation of Co₃O₄-based catalysts

Preparation of Co₃O₄-NPs. Co₃O₄ nanoparticles were prepared by mixing Co³⁺ and Co²⁺ in the presence of ammonia according to literature [43]. Typically, given amounts of Co(NO₃)₂·6H₂O and aqueous ammonia (25 wt%) were mixed together in 50 mL of water in a three-neck flask. A certain amount of H₂O₂ (30 wt%) was then added to the flask and the flask was put into a 60 °C water bath for about 15 min under stirring to complete the oxidization of Co²⁺ to Co³⁺. A corresponding amount of Co(NO₃)₂·6H₂O was dissolved in 20 mL of water to ensure the molar ratio of Co³⁺/Co²⁺ to be 2:1 and the water solution was subsequently poured into the flask. The reaction mixture was stirred for a given time at 60 °C and then cooled down to room temperature. Black precipitates (namely Co₃O₄-NPs) were collected by centrifugation (8000 rpm) and washed with water and ethanol, and further dried at 60 °C for 12 h.

Preparation of Co₃O₄@SiO₂. Typically, about 0.95 g of Co₃O₄-NPs was ultrasonically dispersed into about 5 mL of ethanol in an ice-water bath. After sonicating for several minutes, 1 mL of H₂O, 5 mL of TEOS, and 0.6 mL of aqueous ammonia (25 wt%) were successively added. After another 15 min of ultrasonication, about 0.035 g of carboxymethylcellulose sodium was added to the solution under mechanical stirring. The mixture was further stirred for 4 h at a temperature of 40 °C, and then cooled down to room temperature. Co₃O₄@SiO₂ catalyst was obtained by centrifugation (8000 rpm), washed with water and ethanol, and finally dried at 60 °C for 12 h.

Preparation of Co₃O₄-in-SiO₂. About 0.2 g of Co₃O₄-NPs, 30 mL of methanol and 1.0 g of oleic acid were added into a quartz test tube and the mixture was ultrasonicated for 10 min at room temperature. After methanol was removed from the mixture by distillation, 100 mL of water was added and ultrasonicated for another 40 min. The resulting suspension was then transferred to a 250 mL beaker.

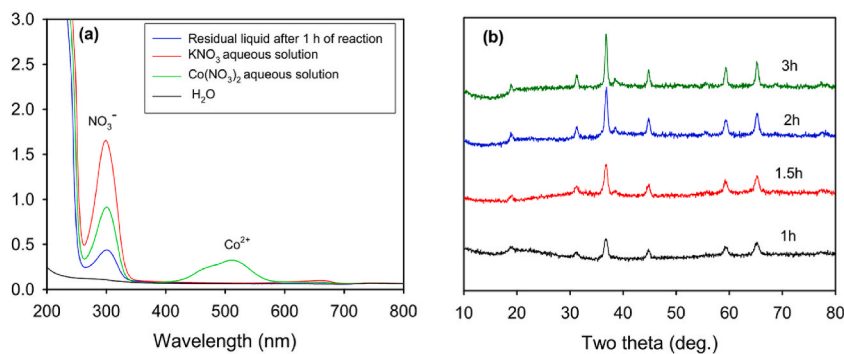


Fig. 1. (a) UV-Vis absorption spectra of the reaction supernatant obtained by centrifugation after 1 h of reaction. For comparison, the UV-Vis absorption spectra of H_2O , $\text{Co}(\text{NO}_3)_2$ and KNO_3 aqueous solutions are also shown. (b) XRD patterns of Co_3O_4 -NPs prepared at different reaction time. ($\text{Co}(\text{NO}_3)_2 \cdot 6\text{H}_2\text{O}$: 0.291 g; $\text{NH}_3 \cdot \text{H}_2\text{O}$: 0.81 mL; and H_2O_2 : 60 μL).

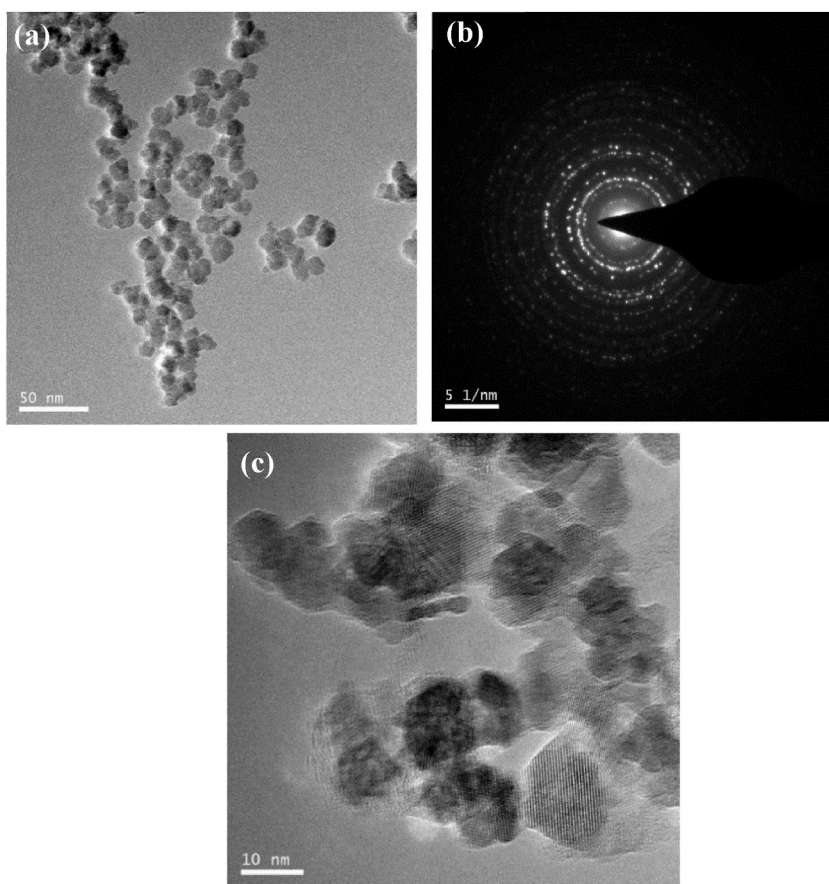


Fig. 2. TEM image (a), electron diffraction pattern (b) and HRTEM image (c) of Co_3O_4 -NPs obtained after 1 h of reaction.

Under magnetic stirring, a mixture of APTES (0.88 mL) and TEOS (6.0 mL) was added dropwise into the above suspension. The suspension was stirred for about 10 min, aged for 2 h, and stirred for another 10 h at room temperature. After that, the suspension was centrifuged at 8000 rpm to obtain a precipitate, followed by washing with water and ethanol, drying at 60 °C for 12 h, and finally calcining at 500 °C for 3 h to produce Co_3O_4 -in- SiO_2 catalyst.

2.3. Catalyst testing

The activity test for methane combustion was conducted in a fixed-bed quartz tubular reactor (internal diameter 6 mm) at

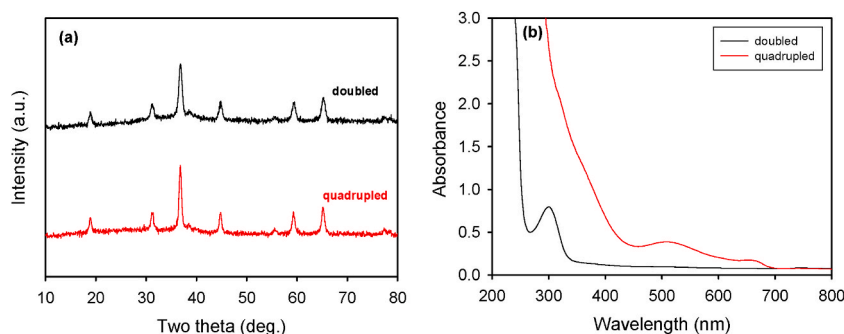


Fig. 3. XRD patterns of Co_3O_4 (a) and UV–Vis absorption spectra of the reaction supernatant (b) obtained after 1 h of reaction when the amounts of reactants were doubled or quadrupled. (Doubled: $\text{Co}(\text{NO}_3)_2 \cdot 6\text{H}_2\text{O}$: 0.582g; $\text{NH}_3 \cdot \text{H}_2\text{O}$: 1.62 mL; H_2O_2 : 120 μL . Quadrupled: $\text{Co}(\text{NO}_3)_2 \cdot 6\text{H}_2\text{O}$: 1.164g; $\text{NH}_3 \cdot \text{H}_2\text{O}$: 3.24 mL; H_2O_2 : 240 μL).

atmospheric pressure. The temperature inside the reactor was measured by a multipoint K type thermocouple placed in the middle of the catalyst bed. The volume composition of the feed gas was 0.5 % CH_4 , 8.0 % O_2 and 91.5 % N_2 . The space velocity was fixed at 12000 $\text{mL} \cdot \text{g}_{\text{Co}_3\text{O}_4}^{-1} \cdot \text{h}^{-1}$. The reactants and products were analyzed on an Echrom A90 gas chromatography equipped with a hydrogen flame ionization detector (FID). The methane conversion was calculated from the inlet and outlet concentration of CH_4 .

2.4. Characterization

The catalyst phase composition was analyzed by X-ray diffraction (XRD), which was performed on a PANalytical X'Pert PRO X-ray diffractometer using $\text{Cu K}\alpha$ X-ray source. The catalyst microstructures were observed using a Tecnai G2 F30 S-Twin transmission electron microscopy (TEM) operating at 300 kV. The nitrogen adsorption and desorption isotherms at 77 K were obtained from a Micromeritics ASAP 2010 sorptometer. The UV–Vis absorption spectra were recorded on a 7600 spectrophotometer (Shanghai Jinghua Technology Instrument Co., Ltd). The amounts of Si were tested by an Oxford Xplora 80 X-ray energy dispersive spectrometer equipped with a SATW window.

3. Results and discussion

3.1. Preparation and characterization of Co_3O_4 catalysts

3.1.1. Co_3O_4 nanoparticles (Co_3O_4 -NPs)

Co_3O_4 -NPs were prepared by mixing Co^{3+} and Co^{2+} (with a molar ratio of $\text{Co}^{3+}/\text{Co}^{2+}$ to be 2:1) in the presence of ammonia. UV–Vis absorption spectra of the reaction supernatant obtained by centrifugation were used to determine whether the reaction was completed or not (Fig. 1a). The absorption peak centered at a wavelength of about 300 nm belongs to the absorption of NO_3^- , whereas the broad absorption in the range of 400–600 nm is related to Co^{2+} in aqueous solution. The absence of the visible light absorption in the spectra (blue line) of the supernatant obtained after 1 h of reaction suggests that the oxidation of Co^{2+} to Co^{3+} is completed under the experimental conditions. Fig. 1b presents the XRD patterns of the solid precipitates obtained at different reaction durations. For all the samples, the peaks at $2\theta = 19.0^\circ$, 31.3° , 36.8° , 38.6° , 44.8° , 55.7° , 59.4° and 65.2° can be all indexed to Co_3O_4 with a cubic spinel structure (space group Fd-3m (227), JCPDS 42-1467) and correspond to the diffractions of {111}, {220}, {311}, {222}, {400}, {422}, {511}, and {440} planes of Co_3O_4 , respectively. The average sizes of Co_3O_4 crystals obtained after reaction for 1 h, 1.5 h, 2 h, and 3 h estimated from the diffraction of {311} plane by Scherrer equation are 12.7 nm, 13.8 nm, 14.1 nm and 14.9 nm respectively, suggesting that the crystal size of Co_3O_4 nanoparticles increases slightly with the increase of reaction time. The TEM image of Co_3O_4 -NPs obtained after 1 h of reaction confirms that they are nano-sized particles with an average diameter of about 13 nm (Fig. 2a). The electron diffraction patterns (Fig. 2b) along with the high resolution TEM (HRTEM) image of Co_3O_4 -NPs (Fig. 2c) reveal their crystalline nature.

In order to improve the quantity of produced Co_3O_4 nanoparticles, the amounts of reactants were doubled or quadrupled with the reaction time being fixed at 1 h, namely the amounts of $\text{Co}(\text{NO}_3)_2 \cdot 6\text{H}_2\text{O}$ (used for formation of Co^{3+}), $\text{NH}_3 \cdot \text{H}_2\text{O}$, and H_2O_2 were, respectively, raised from 0.291 g to 0.582 or 1.164g, from 0.81 mL to 1.62 or 3.24 mL, and from 60 μL to 120 or 240 μL . The XRD patterns of the corresponding products are presented in Fig. 3a. Obviously, all the diffraction peaks can still be indexed to Co_3O_4 with a cubic spinel structure, indicating that the increase in the amount of reactants does not lead to the formation of other cobalt-related phases, e.g., cobalt hydroxides. In addition, the peak width at half height (PWHH) of the {311} plane diffraction peak slightly decreased as the amounts of reactants were quadrupled, suggesting the formation of Co_3O_4 nanoparticles with a relatively large crystal size. However, the observed visible light absorption peak (red line in Fig. 3b) in the UV–Vis absorption spectra of the supernatant after 1 h of reaction indicated that there were still Co^{2+} ions existed in the solution and thus the reaction was not completely finished when the concentrations of reactants were quadrupled. Therefore, the double amounts of reactants were used for the synthesis of Co_3O_4 nanoparticles. The TEM and HRTEM images of Co_3O_4 -NPs obtained in the case of the double amounts of reactants (Fig. 4a and b)

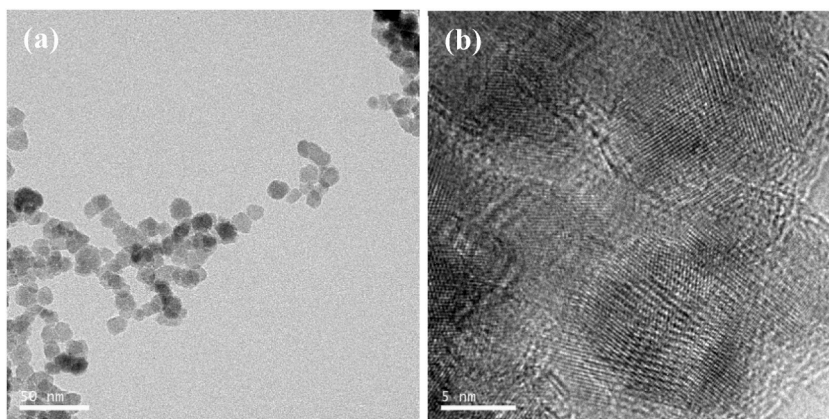


Fig. 4. TEM image (a) and HRTEM image (b) of Co_3O_4 -NPs obtained after 1 h of reaction with the amounts of reactants being doubled.

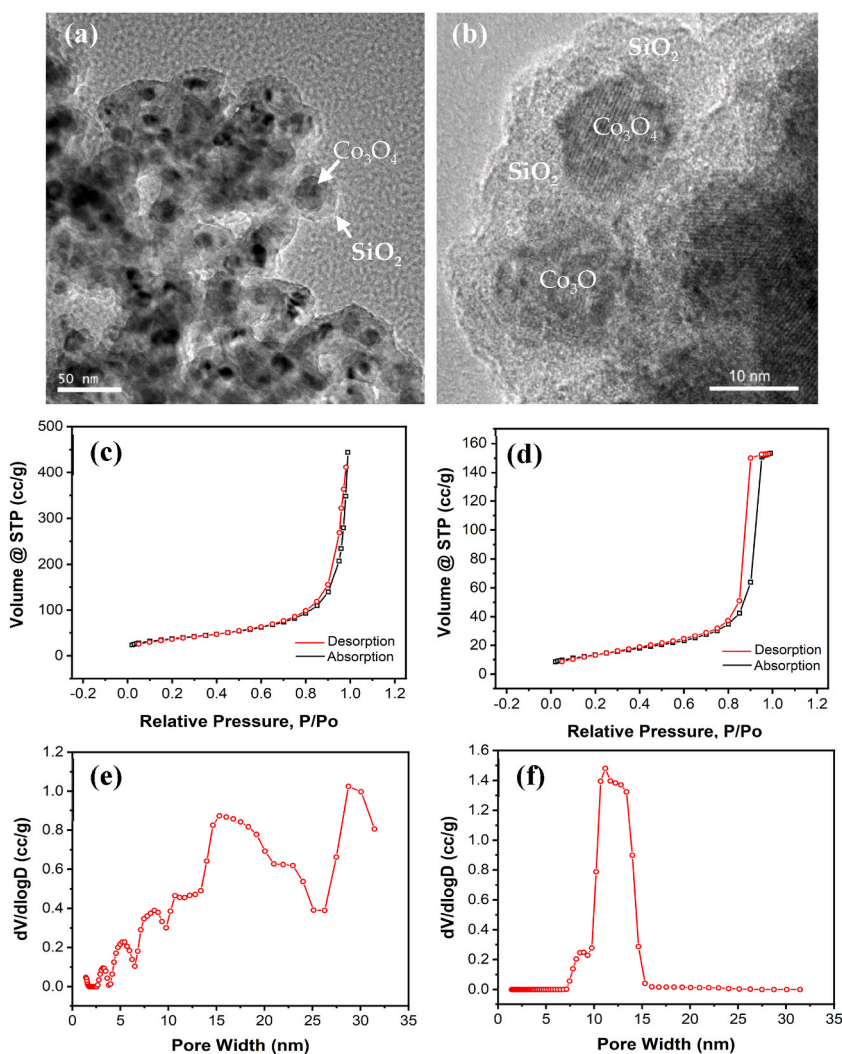


Fig. 5. TEM image (a), HRTEM image (b), nitrogen adsorption and desorption isotherm (c) of Co_3O_4 @ SiO_2 catalyst, and nitrogen adsorption and desorption isotherm of Co_3O_4 -NP catalyst (d), pore size distribution (e) of Co_3O_4 @ SiO_2 catalyst, and pore size distribution of Co_3O_4 -NP catalyst (f). All pore size distributions were derived from the nitrogen adsorption branch of the isotherm using NLDFT model.

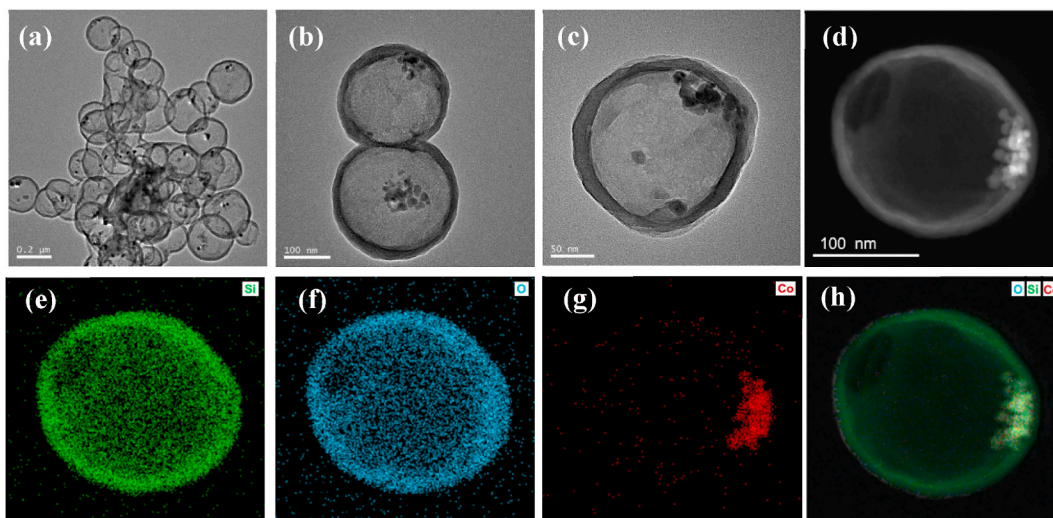


Fig. 6. TEM (a–c) and STEM (d) images of Co_3O_4 -in- SiO_2 . The element mappings of the corresponding Co_3O_4 -in- SiO_2 particle in (d) are shown in (e–h).

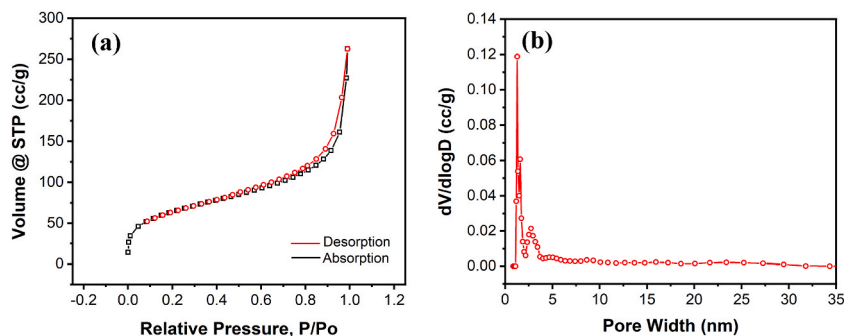


Fig. 7. The nitrogen adsorption and desorption isotherm of Co_3O_4 -in- SiO_2 catalyst (a) and the pore size distribution of Co_3O_4 -in- SiO_2 catalyst derived from the nitrogen adsorption branch of the isotherm using NLDFT model is shown in (b).

confirm that they are nano-sized particles with an average diameter close to that of the Co_3O_4 nanoparticles prepared with the amounts of reactants not being doubled (seen in Fig. 2).

3.1.2. $\text{Co}_3\text{O}_4@/\text{SiO}_2$

The $\text{Co}_3\text{O}_4@/\text{SiO}_2$ catalyst was prepared by an ultrasound-assisted sol-gel method. Fig. 5a and b present the TEM images of $\text{Co}_3\text{O}_4@/\text{SiO}_2$ catalyst. Clearly, the Co_3O_4 nanocrystals are embedded in an amorphous SiO_2 matrix. The thickness of the SiO_2 layer is generally less than 10 nm. In order to determine the pore width of the SiO_2 layer, the pore size distribution of $\text{Co}_3\text{O}_4@/\text{SiO}_2$ was obtained from the nitrogen adsorption branch of the isotherm using NLDFT model (Fig. 5c and e). For comparison, the pore size distribution of unencapsulated Co_3O_4 -NP catalyst was also detected and shown in Fig. 5d and f. For the unencapsulated Co_3O_4 -NP catalyst, no micro-pores are observed and the meso-pores with pore width ranging from 7.5 to 15 nm should come from the nanosized void spaces among the nanoparticles when they pile up. The meso-pores associated with the nanosized void spaces also exist in the $\text{Co}_3\text{O}_4@/\text{SiO}_2$ catalyst and the width of these meso-pores is obviously larger than those in the Co_3O_4 -NP catalyst due to the size of $\text{Co}_3\text{O}_4@/\text{SiO}_2$ nanoparticles is bigger than that of Co_3O_4 -NPs. In addition, meso-pores with pore size less than 7.5 nm, which cannot be observed in unencapsulated Co_3O_4 -NP catalyst, can also be noticed in the $\text{Co}_3\text{O}_4@/\text{SiO}_2$ catalyst (Fig. 5e). These meso-pores should be associated with the SiO_2 layer, implying that the SiO_2 layer is mesoporous.

3.1.3. Co_3O_4 -in- SiO_2

The Co_3O_4 -in- SiO_2 catalyst was prepared by an oleic acid-assisted sol-gel method where the Co_3O_4 nanoparticles were covered with a layer of oleic acid [44]. The role of oleic acid in this method is two-fold: (i) its carboxyl group can react with APTES and thus the hydrolysis and condensation reactions of TEOS may occur at the particle-water interface; (ii) calcination may lead to the removal of oleic acid and the formation of hollow structures. As indicated by the TEM image shown in Fig. 6a, the as-prepared materials indeed display a hollow, spherical structure. The size of these hollow spheres is in the range of 160 nm to about 400 nm. A close examination of

Table 1
Textural and structural properties of the Co_3O_4 catalysts.

Catalyst	BET Surface, ($\text{m}^2\cdot\text{g}^{-1}$)	Pore Volume, ($\text{cm}^3\cdot\text{g}^{-1}$)	Mean Pore Diameter, (\AA)	Si, Theory (wt.%)	Si, Experiment (wt.%)
Co_3O_4 -NPs	49.05	0.24	117	–	–
Co_3O_4 @ SiO_2	132.99	0.69	165	27.3	24.1
Co_3O_4 -in- SiO_2	230.32	0.25	19	41.9	37.6

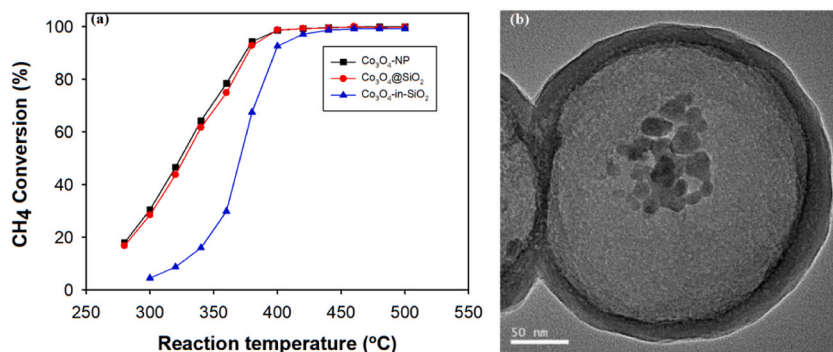


Fig. 8. (a) Catalytic activity for lean methane combustion over different Co_3O_4 -based catalysts and (b) TEM image of a Co_3O_4 -in- SiO_2 particle before reaction.

Table 2
A comparison of the catalytic activities for lean combustion of CH_4 among different Co_3O_4 catalysts.

Catalysts	Composition of reaction mixture	Space velocity ^b ($\text{mL}\cdot\text{g}_{\text{Co}_3\text{O}_4}^{-1}\cdot\text{h}^{-1}$)	T_{50}^a ($^{\circ}\text{C}$)	T_{90}^a ($^{\circ}\text{C}$)	References
Co_3O_4 -NPs	0.5 % CH_4 , 8.0 % O_2 and 91.5 % N_2	12000	325	375	This work
Co_3O_4 @ SiO_2	ditto	12000	328	377	This work
Co_3O_4 -in- SiO_2	ditto	12000	372	398	This work
Co_3O_4 -Ac	ditto	9000	318	385	[29]
Co_3O_4 -Cl	ditto	9000	332	400	[29]
Co_3O_4 -N	ditto	9000	344	416	[29]
Co_3O_4 -S	ditto	9000	367	429	[29]

^a T_{50} or T_{90} is the reaction temperature when the conversion of CH_4 reaches 50 % or 90 %.

^b Space velocity is calculated based on the total gas flow rate.

these hollow spheres (Fig. 6b and c) reveals that the thickness of the shell is close to 20 nm with nanoparticles inside the spheres. The element mappings of hollow spheres confirm that the nanoparticles inside are Co_3O_4 (Fig. 6d–h). The absence of Co_3O_4 nanoparticles on the surface of the hollow spheres indicates the successful synthesis of Co_3O_4 -in- SiO_2 catalyst. However, the absence of the hollow sphere with only one Co_3O_4 nanoparticle inside hints that under current experimental conditions the Co_3O_4 nanoparticles tend to aggregate in the mixture of methanol and oleic acid. In order to examine the pore width of the SiO_2 shell of the spheres, the pore size distribution of Co_3O_4 -in- SiO_2 catalyst was examined from the nitrogen adsorption branch of the isotherm using NLDFT model. As shown in Fig. 7, micro-pores dominate in the SiO_2 shell with a small amount of meso-pores in the width range of 2–4 nm existing, which is significantly different from the pore features of Co_3O_4 @ SiO_2 catalyst.

The textural properties of the three type of catalysts determined by N_2 physical adsorption are summarized in Table 1. The surface area, pore volume and mean pore diameter of Co_3O_4 @ SiO_2 are $49.05 \text{ m}^2 \text{ g}^{-1}$, $0.24 \text{ cm}^3 \text{ g}^{-1}$, 117 \AA , respectively and higher than that of Co_3O_4 -NPs. The different values indicate that the existence of SiO_2 layer promotes the formation of more pores. The pore volume of Co_3O_4 -in- SiO_2 is similar to that of Co_3O_4 -NPs, but its mean pore diameter is smaller, so the BET surface ($230.32 \text{ m}^2 \text{ g}^{-1}$) is larger. The values demonstrate the pore size of SiO_2 layer and catalyst structure are obviously different for the three types of catalyst.

3.2. Performance of Co_3O_4 -based catalysts

3.2.1. A comparison of catalytic activity among three Co_3O_4 catalysts

The catalytic activities of Co_3O_4 -NPs, Co_3O_4 @ SiO_2 , and Co_3O_4 -in- SiO_2 catalysts for the combustion of lean CH_4 are presented in Fig. 8a. TEM image of a Co_3O_4 -in- SiO_2 particle before reaction is shown in Fig. 8b. It is obvious that the presence of a mesoporous SiO_2 layer only slightly influences the catalytic performance of Co_3O_4 nanoparticles. For example, the value of T_{50} or T_{90} over Co_3O_4 -NPs is $325 \text{ }^{\circ}\text{C}$ and $375 \text{ }^{\circ}\text{C}$ respectively, which is just $3 \text{ }^{\circ}\text{C}$ or $2 \text{ }^{\circ}\text{C}$ lower than the corresponding value over Co_3O_4 @ SiO_2 . In particular, among the four Co_3O_4 catalysts prepared using four different cobalt precursors (namely $\text{Co}(\text{C}_2\text{H}_3\text{O}_2)_2$, $\text{Co}(\text{NO}_3)_2$, CoCl_2 , and CoSO_4) [29], both

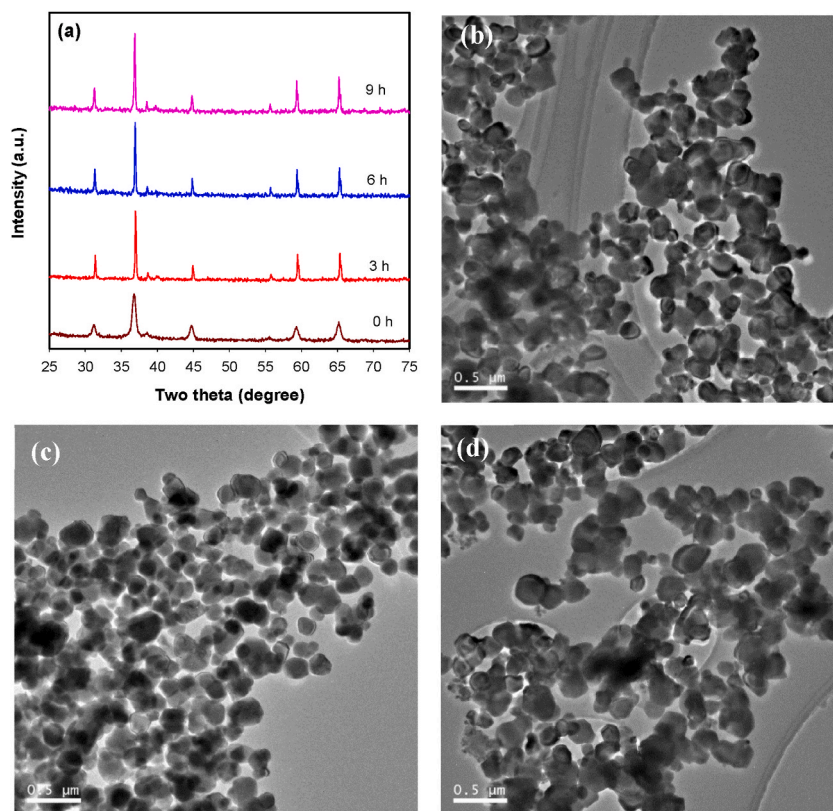


Fig. 9. XRD patterns (a) and TEM images of Co_3O_4 -NP catalyst after calcination at $800\text{ }^\circ\text{C}$ for 3 h (b), 6 h (c), and 9 h (d).

Co_3O_4 -NPs and Co_3O_4 @ SiO_2 show a lower value of T_{90} even at a higher space velocity (seen in Table 2), indicating that Co_3O_4 -NPs and Co_3O_4 @ SiO_2 both exhibit a very good catalytic performance for complete combustion of CH_4 .

As can be seen from Fig. 8a, the catalytic activity of Co_3O_4 -in- SiO_2 catalyst for combustion of lean CH_4 , is lower than that of Co_3O_4 -NPs, especially at low reaction temperatures. The value of T_{50} over Co_3O_4 -in- SiO_2 is, for instance, about $372\text{ }^\circ\text{C}$, much higher than the value of $325\text{ }^\circ\text{C}$ over Co_3O_4 -NPs. To understand the possible reasons for the surprising poor performance of Co_3O_4 -in- SiO_2 , we have re-examined the crystal size of Co_3O_4 nanoparticles in the Co_3O_4 -in- SiO_2 catalyst, and found that the crystal growth of Co_3O_4 nanoparticles occurred during the removal of oleic acid at high temperature. As shown in Fig. 4a, the Co_3O_4 -NPs almost have a uniform particle size with the largest diameter of Co_3O_4 nanoparticles less than 18 nm. As can be clearly seen from Fig. 6b, however, the Co_3O_4 crystals in Co_3O_4 -in- SiO_2 have a relatively wide distribution of diameter with a maximum diameter more than 25 nm (Fig. 6b). This result indicates the occurrence of crystal growth during the removal of oleic acid at calcination temperature of $500\text{ }^\circ\text{C}$, and the increase of crystal size may decrease the catalytic activity of Co_3O_4 nanoparticles. In addition, since the rapid diffusion of the gaseous products (namely CO_2 and H_2O) out of the SiO_2 shell is also important for combustion reaction, it is possible that the relatively poor performance of Co_3O_4 -in- SiO_2 may be partially related to the SiO_2 shell. The effect of pore size and surface area on gas diffusion has been simulated as reported early and proved that the increasing of surface area and decreasing of pore size can significantly weak the gas diffusion [45]. The isotherm characteristics of three kinds of catalysts are different as shown in Fig. 5c, d and 7a. The isotherm morphology of Co_3O_4 -in- SiO_2 is responding to the smaller pore size by comparing to that of Co_3O_4 @ SiO_2 and Co_3O_4 according to the five types of isotherms. As seen in Figs. 5e and 7b, the pore size distribution of mesoporous SiO_2 layer of Co_3O_4 @ SiO_2 is from 2.5 nm to 32.5 nm, meanwhile the pore size distribution of microporous SiO_2 layer of Co_3O_4 -in- SiO_2 is lower than 4 nm. Therefore, compared with the mesoporous SiO_2 layer of Co_3O_4 @ SiO_2 , the SiO_2 shell with micro-pores of Co_3O_4 -in- SiO_2 is expected to be less effective for the gas diffusion and resultantly a negative effect on the CH_4 conversion is generated.

3.2.2. A comparison of thermal stability and lifetime at high reaction temperature between Co_3O_4 -NPs and Co_3O_4 @ SiO_2 catalysts

Since the Co_3O_4 -in- SiO_2 catalyst exhibits a lower catalytic performance compared to Co_3O_4 -NP and Co_3O_4 @ SiO_2 catalysts, we only focus on the thermal stability and lifetime of the latter two catalysts. In order to investigate the thermal stability of the two catalysts, a high calcination temperature at $800\text{ }^\circ\text{C}$ was selected. Fig. 9a illustrates the XRD patterns of the Co_3O_4 -NP catalyst after calcination at $800\text{ }^\circ\text{C}$ for different calcination time. The PWHH of the {311} plane diffraction peak clearly decreased after calcination, indicating a larger crystal size of Co_3O_4 nanoparticles in calcined samples. The TEM images of these samples confirm the sintering phenomenon during calcination, and demonstrate that the size of Co_3O_4 is generally larger than 100 nm, with some particles having a size more than 300 nm (Fig. 9b–d). These results suggest that the Co_3O_4 -NP catalyst has a poor sintering resistance at high temperatures.

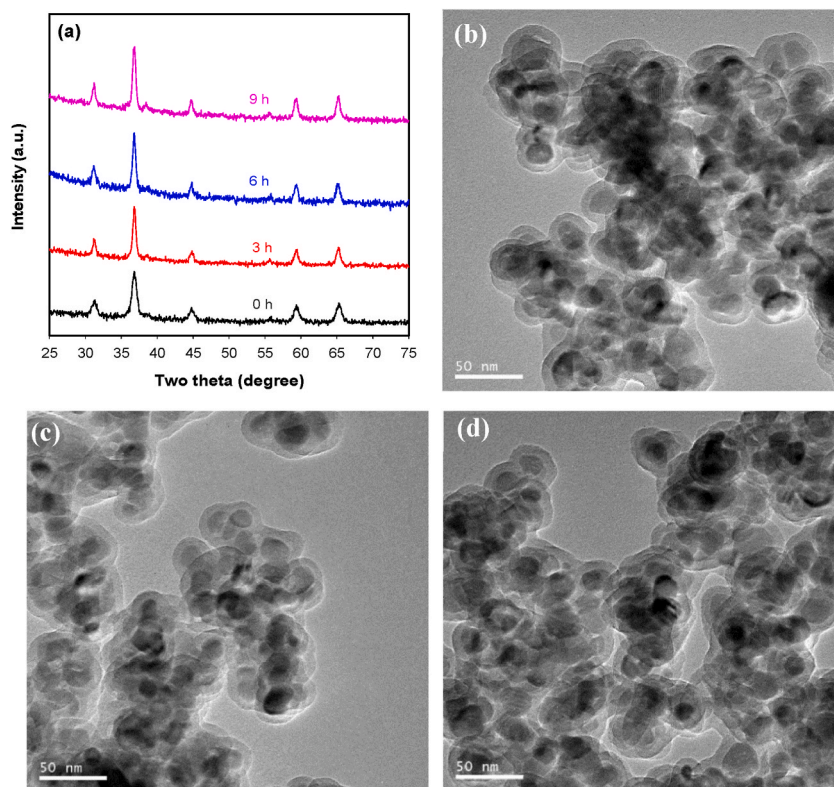


Fig. 10. XRD (a) and TEM images of $\text{Co}_3\text{O}_4@SiO_2$ catalysts after calcination at $800\text{ }^\circ\text{C}$ for 3 h (b), 6 h (c), and 9 h (d). For comparison, the XRD patterns of uncalcinated $\text{Co}_3\text{O}_4@SiO_2$ was also shown in (a).

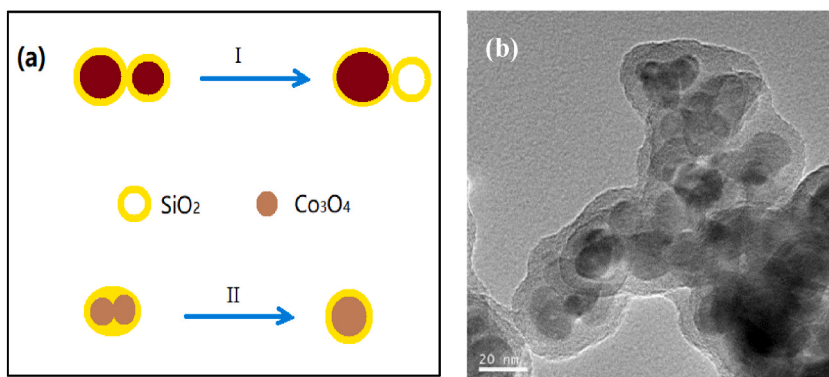


Fig. 11. (a) Scheme of sintering mechanism in the $\text{Co}_3\text{O}_4@SiO_2$ catalyst during calcination and (b) HRTEM image of $\text{Co}_3\text{O}_4@SiO_2$ catalyst after calcination at $800\text{ }^\circ\text{C}$ for 3 h.

In contrast, the $\text{Co}_3\text{O}_4@SiO_2$ catalyst owns a high resistance to sintering. As shown in Fig. 10, even after 9 h of calcination at $800\text{ }^\circ\text{C}$, the average size of Co_3O_4 nanoparticles is still about 20 nm, which implies that the SiO_2 layer may suppress the sintering of Co_3O_4 nanoparticles. It should be pointed out that in comparison with the Co_3O_4 nanoparticles in the uncalcined sample, the crystal size of $\text{Co}_3\text{O}_4@SiO_2$ catalysts grows slowly. This is also supported by the observation that the PWHH of the $\{311\}$ plane diffraction peak after 3 h of calcination reduces slightly, as shown in Fig. 10a. The changes of crystal size of $\text{Co}_3\text{O}_4@SiO_2$ catalysts as a function of calcination time can be nearly negligible according to the TEM images (Fig. 10b–d). The above results indicate that $\text{Co}_3\text{O}_4@SiO_2$ structure enhances the stability and sintering resistance of the $\text{Co}_3\text{O}_4@SiO_2$ catalyst at high temperature.

For the physical structure and sintering mechanism of $\text{Co}_3\text{O}_4@SiO_2$ catalyst, two hypothetical models are considered, as shown in Fig. 11a. Path I shows that every Co_3O_4 nanoparticle is coated with SiO_2 layer separately. When $\text{Co}_3\text{O}_4@SiO_2$ catalysts are sintered at high temperatures, the nanoparticles will keep on growing larger and larger by aggregating more and more $\text{Co}_3\text{O}_4@SiO_2$ nanoparticles

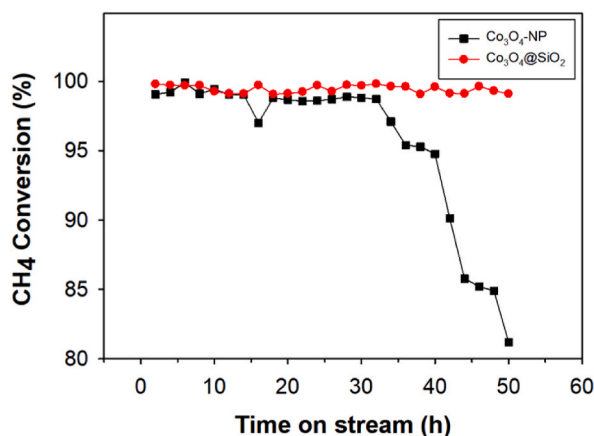


Fig. 12. Catalytic activity for methane combustion as a function of reaction time at 700 °C over Co₃O₄-NP and Co₃O₄@SiO₂ catalysts.

together with the increase of the calcination time according to path I, which disagrees with the TEM results of Co₃O₄@SiO₂ catalysts (Fig. 10b and c). For path II, Co₃O₄ nanoparticles are embedded into one SiO₂ layer. Only limited number of Co₃O₄ nanoparticles within the SiO₂ layer could aggregate to a certain size during the calcination process and no bigger aggregates will appear due to the protection of SiO₂ layer. The second conjecture is consistent with the TEM results of Co₃O₄@SiO₂ catalysts (Fig. 11b). So the above results prove that the second model is probably the sintering mechanism of the Co₃O₄@SiO₂ catalysts.

The lifetimes of two Co₃O₄-NP and Co₃O₄@SiO₂ catalysts are presented in Fig. 12, where a high reaction temperature of 700 °C was chosen to accelerate the deactivation reaction of the catalysts. It is obvious that the Co₃O₄@SiO₂ catalyst possesses a very good stability and the deactivation phenomenon is not observed even after 50 h of reaction. On the contrary, the activity of the Co₃O₄-NP catalyst declines obviously when the reaction time reaches 32 h, and the methane conversion over Co₃O₄-NPs drops from about 100 % to 80 % after 50 h of reaction. These results are undoubtedly associated with the thermal stability of the Co₃O₄ catalysts, namely the deactivation of the Co₃O₄-NP catalyst should be a result of sintering of Co₃O₄ nanoparticles under the reaction conditions, and Co₃O₄ nanoparticles encapsulated in mesoporous SiO₂ may serve as a highly efficient and extraordinarily stable catalyst for the combustion of lean methane.

4. Conclusions

In summary, we have presented a study on three types of Co₃O₄ catalysts (namely Co₃O₄-NPs, Co₃O₄@SiO₂, and Co₃O₄-in-SiO₂) for the combustion of lean methane. The nearly same CH₄ conversion at reaction temperature range of 280–400 °C observed in Co₃O₄-NP and Co₃O₄@SiO₂ catalysts suggests that the presence of mesoporous SiO₂ layer in the Co₃O₄@SiO₂ catalyst almost has no negative effect on the catalytic activity. Compared with Co₃O₄-NPs, however, a much lower CH₄ conversion is found for Co₃O₄-in-SiO₂. The poor performance of Co₃O₄-in-SiO₂ might be related to the crystal growth during the removal of oleic acid via calcination at high temperatures, as well as the microporous SiO₂ shell which is less effective for diffusion of gaseous products. An investigation on both thermal stability and high-temperature activity of Co₃O₄-NP and Co₃O₄@SiO₂ catalysts demonstrates that the presence of the mesoporous SiO₂ layer can significantly improve the sintering resistance of Co₃O₄@SiO₂ and thus the Co₃O₄@SiO₂ catalyst owns a long high-temperature lifetime. These results indicate that the Co₃O₄@SiO₂ catalyst may serve as a highly efficient and extraordinarily stable catalysts for the combustion of lean methane.

Data availability statement

Data will be made available on request.

Ethics approval

Not applicable.

CRedit authorship contribution statement

Panpan Zhang: Conceptualization, Data curation, Formal analysis, Investigation, Methodology, Writing – original draft, Writing – review & editing. **Jinghua Liu:** Formal analysis, Investigation, Methodology, Validation. **Chunjing Zhou:** Data curation, Formal analysis, Investigation. **Zebin Xue:** Data curation, Formal analysis, Investigation. **Yifan Zheng:** Conceptualization, Methodology, Project administration, Resources, Validation. **Haodong Tang:** Conceptualization, Data curation, Methodology, Project administration, Resources, Funding acquisition. **Zongjian Liu:** Conceptualization, Data curation, Formal analysis, Methodology, Project

administration, Resources, Writing – original draft, Writing – review & editing.

Declaration of competing interest

The authors declare that they have no known competing financial interests or personal relationships that could have appeared to influence the work reported in this paper.

References

- [1] C. Zou, Q. Zhao, G.S. Zhang, Bo Xiong, Energy revolution: from a fossil energy era to a new energy era, *NGIB* 3 (2016) 1–11.
- [2] E. Hong, C. Kim, D.H. Lim, H.J. Cho, C.H. Shin, Catalytic methane combustion over Pd/ZrO₂ catalysts: effects of crystalline structure and textural properties, *Appl. Catal., B* 232 (2018) 544–552.
- [3] E. Hong, C. Kim, D.H. Lim, H.J. Cho, C.H. Shin, Catalytic methane combustion over Pd/ZrO₂ catalysts: effects of crystalline structure and textural properties, *Appl. Catal., B* 232 (2018) 544–552.
- [4] Q. Wang, Y. Peng, J. Fu, G.Z. Kyzas, S.M.R. Billah, S. An, Synthesis, characterization, and catalytic evaluation of Co₃O₄/γ-Al₂O₃ as methane combustion catalysts: significance of Co species and the redox cycle, *Appl. Catal., B* 168–169 (2015) 42–50.
- [5] R.W. Howarth, R. Santoro, A. Ingraffea, Methane and the greenhouse-gas footprint of natural gas from shale formations, *Clim. Change* 106 (2011) 679–690.
- [6] M. Sargent, C. Floerchinger, K. McKain, J. Budney, E. Gottlieb, L. Hutrya, J. Rudek, S. Wofsy, Majority of US urban natural gas emissions unaccounted for in inventories, *Proc. Natl. Acad. Sci. USA* 118 (2021), e2105804118.
- [7] X. Feng, L. Jiang, D. Li, S. Tian, X. Zhu, H. Wang, C. He, K. Li, Progress and key challenges in catalytic combustion of lean methane, *J. Energy Chem.* 75 (2022) 173–215.
- [8] B.W. Wang, S. Albarracin-Suazo, Y. Pagan-Torres, E. Nikolla, Advances in methane conversion processes, *Catal. Today* 285 (2017) 147–158.
- [9] G.B. Ariemma, G. Sorrentino, R. Ragucci, M. de Joannon, P. Sabia, Ammonia/methane combustion: stability and NO_x emissions, *Combust. Flame* 241 (2022), 112071.
- [10] N. Zettervall, C. Fureby, E.J.K. Nilsson, Evaluation of chemical kinetic mechanisms for methane combustion: a review from a CFD perspective, *Fuels* 2 (2021) 210–240.
- [11] X. Zhao, Y. Liu, J. Deng, P. Xu, J. Yang, K. Zhang, Z. Han, H. Dai, Mesoporous Pd_kPt alloys: high-performance catalysts for methane combustion, *Mol. Catal.* 442 (2017) 191–201.
- [12] Z. Tang, T. Zhang, D. Luo, Y. Wang, Z. H, R.T. Yang, Catalytic combustion of methane: from mechanism and materials properties to catalytic performance, *ACS Catal.* 12 (2022) 13457–13474.
- [13] G. Löffler, R. Sieber, M. Harasek, H. Hofbauer, R. Hauss, J. Landauf, NO_x formation in natural gas combustion—a new simplified reaction scheme for CFD calculations, *Fuel* 85 (2006) 513–523.
- [14] A. Shafaei, A. Irankhah, Evaluation of Co-Fe, Cu-Fe, Ni-Al and Ni-Fe mixed oxides in catalytic combustion of methane comparison study and investigating the effect of preparation method, *Mol. Catal.* 538 (2023), 112989.
- [15] S. Wang, S. Zhao, Y. Zhang, Y. Wang, Y. Zhang, Y. Zhang, X. Tang, J. Han, E. Duan, Effects of deep eutectic solvent on Cu-Mn-C-O composite catalysts: surface species physical and chemical properties in methane combustion, *Mol. Catal.* 520 (2022), 112161.
- [16] C. Fan, L. Yang, L. Luo, Z. Wu, Z.F. Qin, H.Q. Zhu, W.B. Fan, J.G. Wang, A highly active Pd/H-ZSM-5 catalyst in lean methane combustion prepared via a sol-gel method and treated by reduction-oxidation, *New J. Chem.* 44 (2020) 3940–3949.
- [17] X.B. Feng, L. Jiang, D.Y. Li, S.P. Tian, X. Zhu, H. Wang, C. He, K.Z. Li, Progress and key challenges in catalytic combustion of lean methane, *J. Energy Chem.* 75 (2022) 173–215.
- [18] Y.X. Liu, C.H. Hu, L.C. Bian, Highly dispersed Pd species supported on CeO₂ catalyst for lean methane combustion: the effect of the occurrence state of surface Pd species on the catalytic activity, *Catalysts* 11 (2021) 772.
- [19] S. Kumares, G.W. Lee, M.Y. Kim, On the catalytic combustion behavior of lean methane-air mixture over platinum catalyst with the Navier-Stokes and plug-flow models, *J. Mech. Sci. Technol.* 37 (2023) 2699–2707.
- [20] Z.Y. Tang, T. Zhang, D. Luo, Y.J. Wang, Z. Hu, R.T. Yang, Catalytic combustion of methane: from mechanism and materials properties to catalytic performance, *ACS Catal.* 12 (2022) 13457–13474.
- [21] M. Varbar, S.M. Alavi, M. Rezaei, E. Akbari, Lean methane catalytic combustion over the mesoporous MnO_x-Ni/MgAl₂O₄ catalysts, *Int. J. Hydrog. Energy* 47 (2022) 39829–39840.
- [22] Q.Q. Kong, Y.C. Yin, B. Xue, Y.G. Jin, W.W. Feng, Z.G. Chen, S. Su, C.H. Sun, Improved catalytic combustion of methane using CuO nanobelts with predominantly (001) surfaces, *Beilstein J. Nanotechnol.* 9 (2018) 2526–2532.
- [23] L.H. Hu, Q. Peng, Y.D. Li, Selective synthesis of Co₃O₄ nanocrystal with different shape and crystal plane effect on catalytic property for methane combustion, *J. Am. Chem. Soc.* 130 (2008) 16136–16137.
- [24] Z.P. Chen, S. Wang, W.G. Liu, X.H. Gao, D.N. Gao, M.Z. Wang, S.D. Wang, Morphology-dependent performance of Co₃O₄ via facile and controllable synthesis for methane combustion, *Appl. Catal. A* 525 (2016) 94–102.
- [25] Y.N. Sun, J.W. Liu, J.J. Song, H.H. Huang, N.T. Yang, J. Zhang, Y.H. Sun, Y. Zhu, Exploring the effect of Co₃O₄ nanocatalysts with different dimensional architectures on methane combustion, *ChemCatChem* 8 (2016) 540–545.
- [26] W.D. Hu, J.G. Lan, Y. Guo, X.M. Cao, P. Hu, Origin of efficient catalytic combustion of methane over Co₃O₄ (110): active low-coordination lattice oxygen and cooperation of multiple active sites, *ACS Catal.* 6 (2016) 5508–5519.
- [27] Z. Liu, K. Zhu, A.M. Abed, D. Toghraie, Effect of a palladium catalyst and initial pressure on methane-air catalytic combustion process in a helical coil microchannel: a molecular dynamics approach, *Mol. Catal.* 535 (2023), 112868.
- [28] Y.F. Zheng, Y. Liu, H. Zhou, W.Z. Huang, Z.Y. Pu, Complete combustion of methane over Co₃O₄ catalysts: influence of pH values, *J. Alloys Compd.* 734 (2018) 112–120.
- [29] Y.F. Zheng, Y.Q. Yu, H. Zhou, W.Z. Huang, Z.Y. Pu, Combustion of lean methane over Co₃O₄ catalysts prepared with different cobalt precursors, *RSC Adv.* 10 (2020) 4490–4498.
- [30] Z.Y. Pu, H. Zhou, Y.F. Zheng, W.Z. Huang, X.N. Li, Enhanced methane combustion over Co₃O₄ catalysts prepared by a facile precipitation method: effect of aging time, *Appl. Surf. Sci.* 410 (2017) 14–21.
- [31] J.J. Yang, J.Q. Wang, J.J. Zhao, Y. Bai, H.R. Du, Q. Wang, B. Jiang, H.X. Li, CO₂ conversion via dry reforming of methane on a core-shell Ru@SiO₂ catalyst, *J. CO₂ Util.* 57 (2022), 101893.
- [32] K.H. Han, S. Wang, N. Hu, W.D. Shi, F.G. Wang, Alloying Ni-Cu nanoparticles encapsulated in SiO₂ nanospheres for synergistic catalysts in CO₂ reforming with methane reaction, *ACS Appl. Mater. Interfaces* 14 (2022) 23487–23495.
- [33] S. Yoo, E.W. Lee, D.H. Kim, Methane combustion over mesoporous cobalt oxide catalysts: effects of acid treatment, *Mol. Catal.* 511 (2021), 111728.
- [34] Y. Jiang, W. Li, K. Chen, X. Zhang, C. Shen, L. Yuan, A rod-like Co₃O₄ with high efficiency and large specific surface area for lean methane catalytic oxidation, *Mol. Catal.* 522 (2022), 112229.
- [35] A. Efreanova, T. Rajkumar, A. Szamosvölgyi, A. Sági, K. Baán, I. Szent, J.G. Pérez, G. Varga, J. Kiss, G. Halasi, Á. Kukovecz, Z. Kónya, Complexity of a Co₃O₄ system under ambient-pressure CO₂ methanation: influence of bulk and surface properties on the catalytic performance, *J. Phys. Chem. C* 125 (2021) 7130–7141.

- [36] A. Efremova, I. Szent, J. Kiss, Á. Szamosvölgyi, A. Sági, K. Baán, L. Olivi, G. Varga, Z. Fogarassy, B. Pécz, Á. Kukovecz, Z. Kónya, Nature of the Pt-cobalt-oxide surface interaction and its role in the CO₂ methanation, *Appl. Surf. Sci.* 571 (2022), 151326.
- [37] L. Gucci, G. Boskovic, E. Kiss, Bimetallic cobalt based catalyst, *Catal. Rev.* 52 (2010) 133–203.
- [38] Z. Ferencz, K. Baán, A. Oszkó, Z. Kónya, T. Kecskés, A. Erdőhelyi, Dry reforming of CH₄ on Rh doped Co/Al₂O₃ catalysts, *Catal. Today* 228 (2014) 123–130.
- [39] E. Varga, K. Baán, G.F. Samu, A. Erdőhelyi, A. Oszkó, Z. Kónya, J. Kiss, The effect of Rh on the Interaction of Co with Al₂O₃ and CeO₂ supports, *Catal. Lett.* 146 (2016) 1800–1807.
- [40] G. Varga, A. Sági, T. Varga, K. Baán, I. Szent, G. Halasi, R. Mucsi, L. Óvári, J. Kiss, Z. Fogarassy, B. Pécz, Á. Kukovecz, Z. Kónya, Ambient pressure CO₂ hydrogenation over a cobalt/manganese-oxide nanostructured interface: a combined in situ and ex situ study, *J. Catal.* 386 (2020) 70–80.
- [41] C. Andoni, B.D. Rivas, J.I.G. Ortiz, R.L. Fonseca, Bulk Co₃O₄ for methane oxidation: effect of the synthesis route on physico-chemical properties and catalytic performance, *Catalysts* 12 (2022) 87.
- [42] A. Choya, B.D. Rivas, J.R.G. Velasco, J.I.G. Ortiz, R.L. Fonseca, Oxidation of residual methane from VNG vehicles over Co₃O₄-based catalysts: comparison among bulk, Al₂O₃-supported and Ce-doped catalysts, *Appl. Catal., B* 237 (2018) 844–854.
- [43] J.L. Dong, L.N. Song, J.J. Yin, W.W. He, Y.H. Wu, N. Gu, Y. Zhang, Co₃O₄ nanoparticles with multi-enzyme activities and their application in immunohistochemical assay, *ACS Appl. Mater. Interfaces* 6 (2014) 1959–1970.
- [44] K. Fujiwara, Y. Kuwahara, Y. Sumida, H. Yamashita, Fabrication of photocatalytic paper using TiO₂ nanoparticles confined in hollow silica capsules, *Langmuir* 33 (2017) 288–295.
- [45] Y.L. Chen, L.Y. Cao, W. He, R. He, Effects of pore characteristics of fractal porous media on gas diffusion, *CIE J.* 62 (2011) 3024–3029.